

---

# UGCANET: A UNIFIED GLOBAL CONTEXT-AWARE TRANSFORMER-BASED NETWORK WITH FEATURE ALIGNMENT FOR ENDOSCOPIC IMAGE ANALYSIS

---

A PREPRINT

**Pham Vu Hung**

School of Information and Communication Technology  
Hanoi University of Science and Technology  
hung.pv194069@sis.hust.edu.vn

**Nguyen Duy Manh**

School of Information and Communication Technology  
Hanoi University of Science and Technology  
manh.nd202657m@sis.hust.edu.vn

**Nguyen Thi Oanh**

School of Information and Communication Technology  
Hanoi University of Science and Technology  
oanhnt@soict.hust.edu.vn

**Nguyen Thi Thuy**

School of Science, Engineering and Technology  
RMIT University  
thuy.nguyen43@rmit.edu.vn

**Dinh Viet Sang \***

School of Information and Communication Technology  
Hanoi University of Science and Technology  
sangdv@soict.hust.edu.vn

July 13, 2023

## ABSTRACT

Gastrointestinal endoscopy is a medical procedure that utilizes a flexible tube equipped with a camera and other instruments to examine the digestive tract. This minimally invasive technique allows for diagnosing and managing various gastrointestinal conditions, including inflammatory bowel disease, gastrointestinal bleeding, and colon cancer. The early detection and identification of lesions in the upper gastrointestinal tract and the identification of malignant polyps that may pose a risk of cancer development are critical components of gastrointestinal endoscopy's diagnostic and therapeutic applications. Therefore, enhancing the detection rates of gastrointestinal disorders can significantly improve a patient's prognosis by increasing the likelihood of timely medical intervention, which may prolong the patient's lifespan and improve overall health outcomes. This paper presents a novel Transformer-based deep neural network designed to perform multiple tasks simultaneously, thereby enabling accurate identification of both upper gastrointestinal tract lesions and colon polyps. Our approach proposes a unique global context-aware module and leverages the powerful MiT backbone, along with a feature alignment block, to enhance the network's representation capability. This novel design leads to a significant improvement in performance across various endoscopic diagnosis tasks. Extensive experiments demonstrate the superior performance of our method compared to other state-of-the-art approaches.

## 1 Introduction

Digestive tract diseases, particularly colorectal cancer, pose a significant threat to human health [1]. Accurate diagnosis and classification of these diseases are critical for effective treatment and improvement of patient outcomes [2]. Despite

---

\*Corresponding author

the increasing incidence of these diseases, manual analysis by expert physicians is still the gold standard for diagnosis and classification. However, this method is time-consuming and subject to human error [3].

Recent advancements in computer-aided diagnosis (CAD) have demonstrated considerable potential in enhancing the precision of disease classification [4]. A notable technique in this regard is polyp segmentation, which aims to accurately identify and isolate lesions in images of the digestive tract [5]. The extracted information can subsequently aid in diagnosing and classifying digestive tract diseases, including potential precursors to cancer. It is imperative to examine the stomach and its relevant structures thoroughly. These cutting-edge advancements are poised to revolutionize disease detection and diagnosis in the medical field.

Accurate anatomical site classification is a crucial aspect of medical image analysis [6, 7, 8], enabling the identification of specific structures within the human body. This information is essential for precise diagnosis and effective treatment planning, providing invaluable insights into areas of anomalies or lesions. Recent advancements in deep learning techniques have contributed significantly to the field of anatomical site classification [6, 7, 8]. Nonetheless, challenges persist due to the variability of imaging modalities and the inherent complexity of the human anatomy. Overcoming these hurdles is vital for advancing medical image analysis and improving patient outcomes.

Accurate classification of lesions and *Helicobacter pylori* (HP) has garnered increasing attention in the medical field. Lesion classification is crucial in improving diagnoses and treatments for various medical conditions. Image segmentation is sometimes necessary to understand the lesion or polyp location clearly. Polyp segmentation is particularly valuable in the early detection of digestive tract diseases. Manual analysis of medical images is prone to human error and time-consuming, highlighting the need for automated methods. Our study focuses on classification and segmentation, with findings indicating their equal significance and mutual complementarity.

In this paper, we propose a new model that can well solve two tasks at the same time. The experimental results demonstrate superior performance of our model in both single-task and multi-task learning scenarios. Our main contributions are:

- We identified that the existing MiT backbone needed to adequately leverage the channel attention mechanism, resulting in the loss of context information in deeper layers. To overcome this, we incorporated the CGNL module with channel attention in groups to establish local relationships between channel groups.
- However, relationships between groups were still lacking, prompting us to add the SE module to bridge the gap between the groups. The combination of these two modules enhanced the channel characteristics.
- By combining these two contributions, we present UGCANet, which can extensively leverage the channel attention mechanism and propagate through the FaPN decoder [9], resulting in segmented output. Additionally, the Fully-connected layer processes some of the feature information to address the classification task.

The remaining sections of the paper are structured as follows. We briefly review related work in Section 2. Then, we present our proposed method in Section 3. In Section 4, we showcase the conducted experiments and discuss results. Finally, we conclude the paper and discuss potential future directions in Section 5.

## 2 Related work

### 2.1 Deep learning and medical image segmentation

**Deep learning.** Deep learning has been widely used in various fields, such as computer vision, natural language processing, and speech recognition. In recent years, deep learning has made significant progress in these fields and has been applied to various tasks, including image classification, object detection, and segmentation. In the field of image classification, Convolutional Neural Networks (CNNs) have proven to be highly effective in achieving impressive results on large-scale image classification datasets, such as ImageNet [10], CIFAR-100 [11]. This highlights the significance of these models as a benchmark for deep learning and image classification research. The advancements in CNNs have paved the way for continued progress in both fields and serve as a foundational foundation for future research [12, 13]. Densenet [12] uses dense blocks, where each layer receives inputs from all previous layers in the block. This helps reduce the vanishing gradient problem and makes it easier for the network to propagate information through the network. In ResNet [13], the network learns residual connections instead of trying to directly learn the desired mapping from inputs to outputs. Subsequently, in the ensuing years, there have been continued advancements in image classification and deep learning. A new method for scaling CNNs that is more efficient and effective than traditional methods. The method, called EfficientNet, balances the trade-off between accuracy and computational cost by scaling the network’s depth, width, and resolution in a consistent manner. The authors show that EfficientNet outperforms previous state-of-the-art models on several benchmark datasets for image classification [14]. The progression has not stopped at that point. A breakthrough as the first transformers architecture appeared when the attention

mechanism was first introduced by [15]. The introduction of the attention mechanism had a significant impact on the thinking of computer vision researchers, leading to the utilization of the self-attention mechanism in computer vision and the emergence of transformer-based proposals for machine vision.

The Vision Transformer (ViT) demonstrates remarkable performance compared to cutting-edge CNNs and requires significantly fewer computational resources for training [16]. Unlike traditional CNNs, In ViT [16], the input image is first divided into a sequence of non-overlapping patches, which are then treated as tokens. Which allows the network to focus on different regions of the input image when making predictions. While ViT is effective for image classification, adapting it for dense predictions at the pixel level, like object detection and segmentation, presents a significant challenge. The Pyramid Vision Transformer (PVT) [17] is introduced as a solution to that issue through the creation of a shrinking pyramid and the implementation of spatial-reduction attention (SRA). Focal [18] used a new mechanism called Focal Self-attention that incorporates both fine-grained local and coarse-grained global interactions, CaiT emphasized the significance of utilizing Layer-scale to scale up the depth dimension [19], LeViT [20] astutely applied a combination of CNNs and Transformers to create a novel hybrid neural network, resulting in both precise and rapid inference. While ViT and PVT can be limited by distant dependent information DAT [21] introduced deformable self-attention module select key-value pairs depending on the data.

**Medical image segmentaton.** Unet [22] has gained popularity in medical image segmentation. The model is designed to handle tasks with multiple scales and uses a combination of downsampling and upsampling layers to maintain high resolution in the segmented output. The key feature of Unet is its symmetrical architecture, which allows for precise localization and preservation of fine details in the segmented image. However, it has a few limitations. One of the main limitations is that it may struggle with small or fine structures, such as tiny vessels or tumors, in medical images. Additionally, the symmetrical architecture of Unet can lead to a lack of context information and decreased performance in complex or large-scale segmentation tasks. In order to address these limitations, Unet++ [23] and DoubleUnet [24] were proposed. Unet++ introduces a multi-scale learning mechanism, which helps capture contextual information from different scales. This leads to improved performance for small and fine structures in medical images. DoubleUnet, on the other hand, uses two parallel Unets, each with different levels of abstraction and context, to make predictions. This dual-stream approach helps the model capture local and global context information, improving performance in complex and large-scale segmentation tasks. Several models are based on Unet and Transformers, like TransUnet [25] and TransFuse [26]. The Hybrid ViT component of TransUNet stacks the CNN and Transformer together, leading to high computational costs. However, this also improves accuracy and performance compared to using either model individually. TransFuse is designed to address the high computational costs of TransUNet. TransFuse utilizes a parallel architecture, which allows it to reduce the computational overhead of the Transformer and CNN components of the network. In TransFuse, the Transformer and CNN components are trained in parallel, allowing faster and more efficient training. The parallel architecture also allows for more efficient use of hardware resources, such as GPUs, which can result in faster and more efficient inference.

## 2.2 Lesion Segmentation for endoscopy

Gastrointestinal (GI) lesion segmentation is crucial in early detection and diagnosis of digestive tract diseases such as esophageal cancer, duodenal ulcer, and colorectal cancer. In recent years, many deep learning-related works have been published in this area. CNN models such as Unet [22] or Unet++ [23] utilize skip connections to mitigate information loss caused by stacking numerous convolutional layers. The Unet architecture enhances the overall visibility of the model and enables the integration of multi-scale information. In 2022, Manh et al. [27] proposed an Unet-based multi-tasking model called EndoUnet to simultaneously solve multiple upper GI tasks. Supplementary modules are also a way to enrich information representation, ASPP [28] expanded the field of view to a larger perceptual area, making it suitable for capturing broader contexts. PraNet [29] adds an RFB module [30] helps generate features with the different receptive fields. Another approach to enhance the representation of information is utilizing the attention module. EncNet [31], DFN [32] use attention in the feature map’s channel dimension to consider the global context, such as the occurrence of different classes in context. CCBANet [33] proposed an Attention Balance module (BAM). BAM uses an attention mechanism for three distinct regions: the background, polyp, and boundary. BAM intensifies local context information when retrieving features from the encoder block.

## 2.3 Image classification for endoscopy

Although GI endoscopic image documentation is an economical and effective solution for endoscopic reporting, implementing computer-assisted techniques for quality control poses a challenge due to the resemblance of appearance between different anatomical sites and the considerable and inconsistent variability in site appearance across patients.

In 2018, a GoogLeNet-based diagnostic program [34] was developed to recognize the anatomical site from 27335 endoscopic images of four major categories (larynx, esophagus, stomach, and duodenum). The CNN is also utilized in disease detection; Lin et al. [35] modified Inception V3 to recognize Helicobacter Pylori infection and obtained relatively satisfactory results (accuracy of 95%). In 2019, a system called WISENSE [36], which is based on deep learning and reinforcement learning, was proposed by Wu et al. for real-time blind-spot monitoring, timing the procedure, and classifying anatomical sites. In this study, the authors implemented the 27-class protocol, which includes 26 anatomical sites and a NA class for images that cannot be classified to any site. By combining data collection, automatic ROI extraction, and a CNN-based model, He et al. [37] presented a comprehensive workflow for EGD image classification in 2020.

### 3 Method

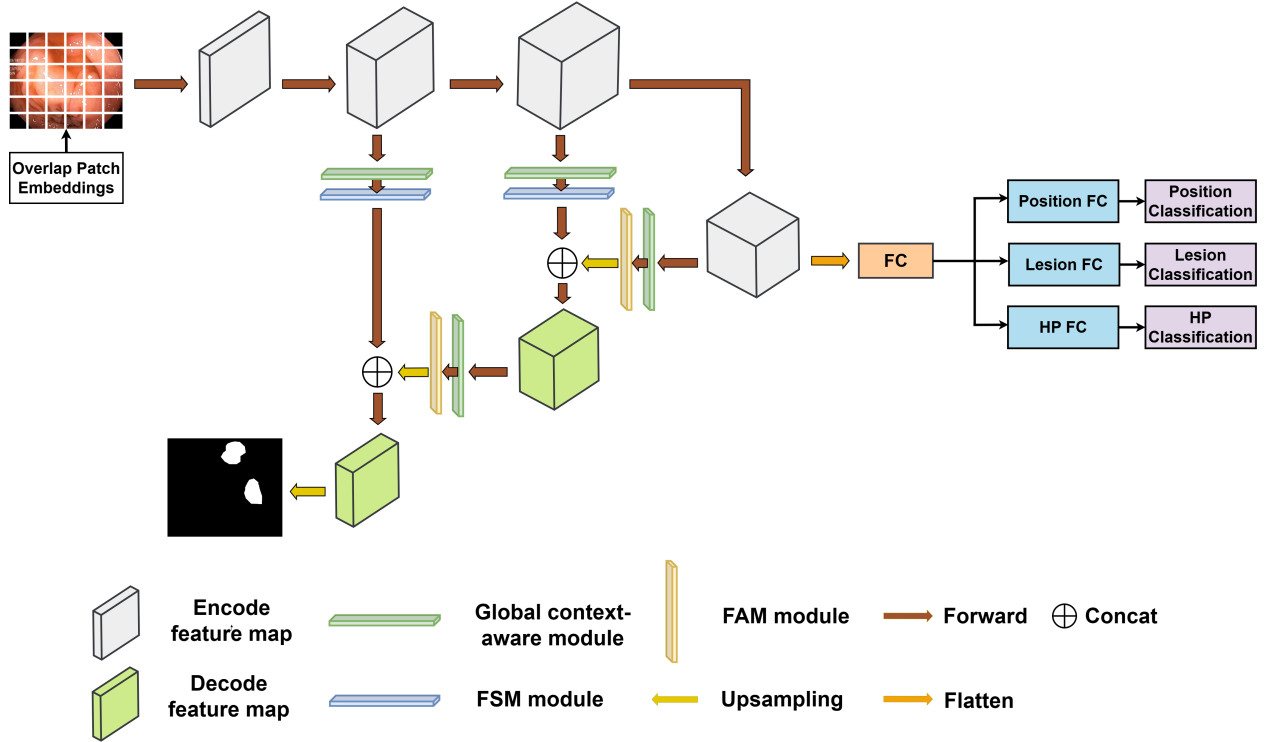


Figure 1: UGCANet architecture

#### 3.1 Overview

The architecture of our proposed network, UGCANet, is illustrated in Fig. 1. Our model uses the encoder-decoder design. The encoder is capable of acquiring a shared feature representation that is proficient in serving multiple tasks, producing four intermediate feature maps, and transmitting the final three to the CGNL [38] and module SE [39] to aggregate context information then a branch will undergo the average pooling layer and three FC layer to generate the classification labels for our tasks. Additionally, it will pass through the FaPN [9] module to generate the prediction output for the segmentation task.

#### 3.2 Backbone

MiT [40] improves upon ViT [16] by introducing hierarchical feature representation, overlapped patch merging, efficient self-attention, and Mix-FFN. The hierarchical feature representation generates multi-level features with different resolutions. Each hierarchical feature map  $F_i$  has a resolution of  $\frac{H}{2^{i+1}} \times \frac{W}{2^{i+1}} \times C_i$ , where  $i$  belongs to the set  $\{1, 2, 3, 4\}$  and  $C_i$  increases with each level. While overlapped patch merging preserves local continuity in image patches. Efficient self-attention reduces computational load by using a reduction ratio. Mix-FFN mitigates the impact of zero padding on location information leakage, improving accuracy.

### 3.3 Global Context-Aware Modules

#### 3.3.1 Compact Generalized Non-Local

The Compact Generalized Non-Local (CGNL) [38] module is a computer vision technique that models how different positions of an image interact across channels. Unlike the Non-Local module [41], CGNL applies distinct weights to each channel by first flattening the feature outputs after linear transformation layers. By using separate weights for each channel, it can better capture the underlying relationships between different parts of an image, leading to improved accuracy. CGNL stands out from channel attention modules due to the computational load required. Through the application of Taylor expansion, Yue et al. [38] are able to approximate the complex calculations required by the module with a simpler polynomial function. This makes the computation more efficient and helps to reduce the overall computational cost of the CGNL module.

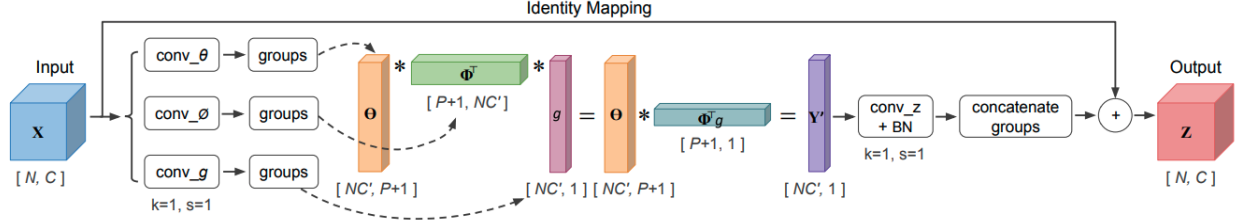


Figure 2: Grouped compact generalized non-local (CGNL) module [38].

#### 3.3.2 Squeeze and Excitation

Squeeze and Excitation (SE) [39] is a neural network building block that improves the incantational power of CNNs by explicitly modeling interdependencies between channels of feature maps. The SE block consists of two main operations: the squeeze and excitation operations.

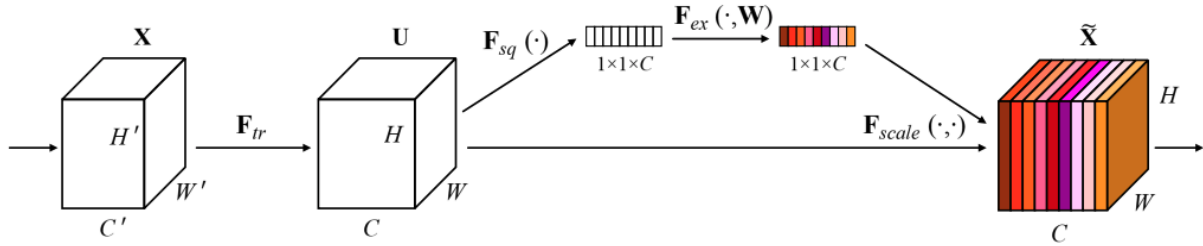


Figure 3: A Squeeze-and-Excitation block [39].

In the squeeze operation, a global spatial pooling operation is applied to the feature maps, which aggregates the information across spatial locations.

In the excitation operation, the channel-wise statistics obtained from the squeeze operation are used to compute a set of learnable weights. These weights are then used to modulate the feature maps through a gating mechanism, which assigns higher weights to informative channels and lower weights to less informative ones. The gating mechanism is typically implemented as a sigmoid or ReLU activation function.

Because of its simple and efficient design, it can be stacked multiple times to form a deep network.

### 3.4 Decoder

In the encoder-decoder architecture, the problem of object information loss can be particularly challenging for small objects in the image. Because the encoder compresses the image features into a lower-dimensional space, which can result in the loss of fine-grained details and spatial information. This can lead to reduced segmentation performance, especially in scenarios where small objects are of great importance, such as medical image analysis.

Huang et al. introduced the Feature-aligned Pyramid Network (FaPN) [9], which is a new feature-aligned pyramid network for dense image prediction. The FaPN model addresses the issue of feature misalignment in the encoder-

decoder architecture by using a feature alignment module that aligns the features extracted at different levels of the network.

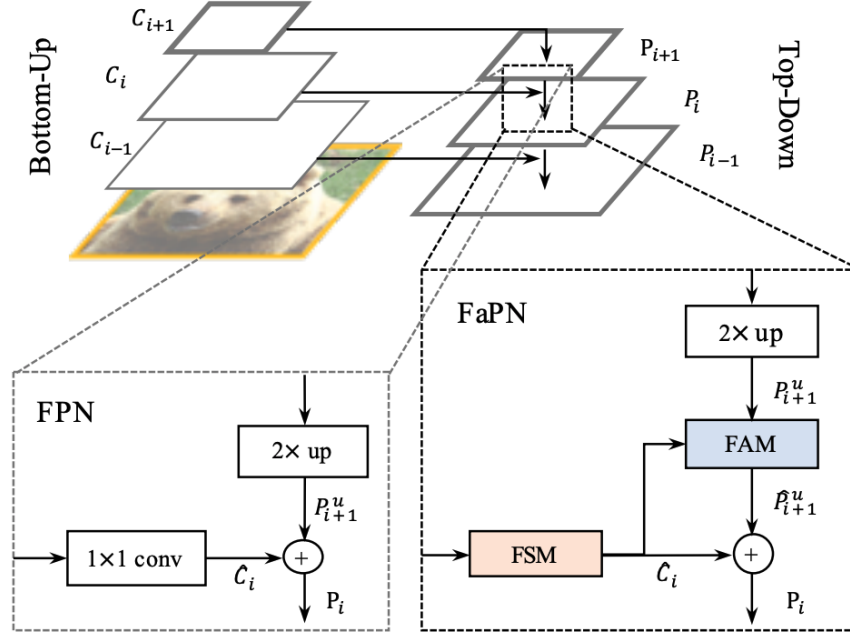


Figure 4: Overview comparison between FPN and FaPN [9].

**Feature Alignment Module:** The downsampling operations in the encoder-decoder architecture result in a misalignment between the feature maps of the encoder and decoder. This misalignment can cause issues when fusing the features through addition or concatenation near object boundaries.

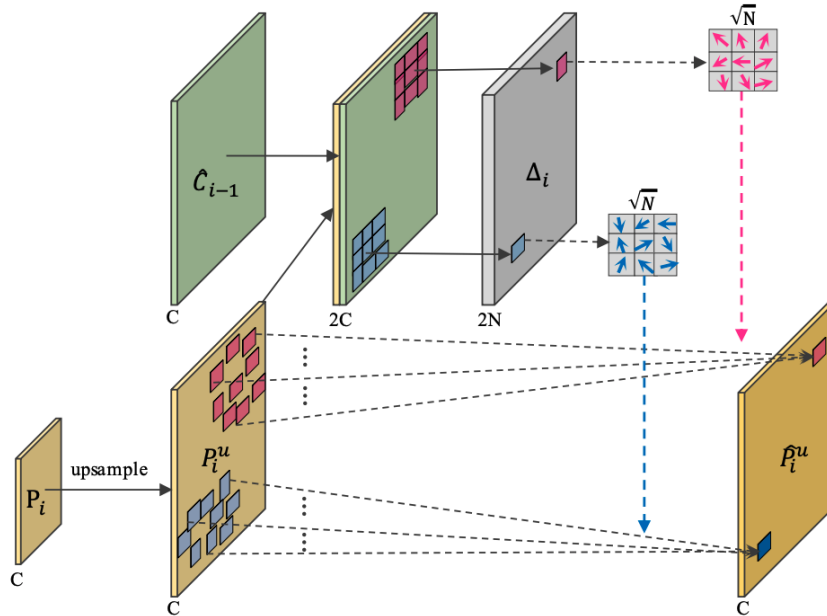


Figure 5: Feature alignment module [9]

To address this, Feature Alignment Module (FAM) used deformable convolution and learnable offset fields to adjust the convolutional sample locations, which helps preserve accurate object boundaries.

**Feature Selection Module:** Rather than employing a  $1 \times 1$  convolution to reduce the channel dimension of intricate features, FSM (Feature Selection Module) adopts a weight assignment approach for feature maps. The FSM architecture is motivated by the SE module but differs in that it includes an additional shortcut between the input and scaled feature maps. This unique shortcut enables FSM to effectively enhance multi-scale feature aggregation.

### 3.5 Loss

In our study, we evaluate two different types of datasets, including Upper GI and polyp data. In each task, we define a different type of loss to match the context.

#### 3.5.1 Loss for Colonoscopy

Our loss function for this task is defined as:

$$\mathcal{L} = \mathcal{L}_{BCE}^w + \mathcal{L}_{IoU}^w \quad (1)$$

where  $\mathcal{L}_{BCE}^w$  is weighted binary cross-entropy and  $\mathcal{L}_{IoU}^w$  is weighted IoU loss. Thus,  $\mathcal{L}$  is called weighted BCE and IoU loss. In contrast to the standard binary cross-entropy loss function, the  $\mathcal{L}_{BCE}^w$  assigns higher weights to hard pixels rather than treating all pixels equally. As for  $\mathcal{L}_{IoU}^w$ , increases the weights of hard pixels to emphasize their importance.

#### 3.5.2 Loss for upper GI tract

We collect data from various sources to train our models, which we combine to create a comprehensive training dataset. However, in this merged dataset, each sample is only relevant to a subset of the tasks. To clarify the type of sample, we use  $\mu_i^t \in \{0, 1\}$  as the indicator, with  $t \in \{pos, le, hp, seg\}$  representing the tasks of anatomical site classification, lesion type classification, HP classification, and lesion segmentation, respectively. Suppose that  $\mathbf{y}_i^t$  is the one-hot encoding of the label of the  $i$ -th sample in the  $t$ -th task. Assuming  $\hat{\mathbf{y}}_i^t$  be the probabilistic output of the  $i$ -th sample in the  $t$ -th task. If  $t \in \{pos, le, hp\}$  then  $\mathbf{y}_i^t$  and  $\hat{\mathbf{y}}_i^t$  are vectors whose length equals the number of classes, let  $C_{pos}$  represent the number of anatomical sites,  $C_{le}$  represent the number of lesion classes (including five lesion types and a negative one), and  $C_{hp}$  represent whether the HP sample is positive or not. Specifically,  $C_{pos} = 10$ ,  $C_{le} = 6$ , and  $C_{hp} = 1$ . If  $t = seg$ , then both  $\mathbf{y}_i^t$  and  $\hat{\mathbf{y}}_i^t$  are two-dimensional matrices with dimensions equal to those of the input images.

The loss function  $\mathcal{L}_{pos}$ , used for the task of classifying anatomical sites, is a type of multi-class cross-entropy loss and is defined as follows:

$$\mathcal{L}_{pos} = - \sum_{i=1}^N \left( \mu_i^{pos} \sum_{j=1}^{C_{pos}} y_i^{pos}(j) * \log \hat{y}_i^{pos}(j) \right) \quad (2)$$

where  $N$  is the number of training samples.

The loss  $\mathcal{L}_{le}$  for lesion type classification task is another multi-class cross-entropy loss defined as follows:

$$\mathcal{L}_{le} = - \sum_{i=1}^N \left( \mu_i^{le} \sum_{j=1}^{C_{le}} y_i^{le}(j) * \log \hat{y}_i^{le}(j) \right) \quad (3)$$

The loss  $\mathcal{L}_{hp}$  for HP classification is the binary cross-entropy loss defined as follows:

$$\mathcal{L}_{hp} = - \sum_{i=1}^N \mu_i^{hp} * \left( y_i^{hp} * \log \hat{y}_i^{hp} + (1 - y_i^{hp}) * \log (1 - \hat{y}_i^{hp}) \right) \quad (4)$$

The total loss is a weighted combination of the above loss functions. This is defined as follows:

$$\mathcal{L}_{total} = \lambda_1 * \mathcal{L}_{pos} + \lambda_2 * \mathcal{L}_{le} + \lambda_3 * \mathcal{L}_{hp} + \lambda_4 * \mathcal{L}_{seg} \quad (5)$$

where  $\lambda_t$  indicates the importance level of the  $t$ -th task. In our work, we set  $\lambda_1 = \lambda_2 = \lambda_3 = \lambda_4 = 1$ .

## 4 Experiments

### 4.1 Datasets

Our model is evaluated on two gastrointestinal datasets: one consists of images of the upper gastrointestinal tract, and the other is polyp data.

#### 4.1.1 Colonoscopy dataset

For the task of polyp segmentation, we conducted our evaluation using a total of 5 datasets. Below, we provide detailed information about each of these datasets.

**Kvasir dataset** [42]: This dataset comprises 1000 images with varying resolutions ranging from  $720 \times 576$  to  $1920 \times 1072$  pixels. Kvasir data is collected using endoscopic equipment at Vestre Viken Health Trust (VV) in Norway, annotated and verified by medical doctors (experienced endoscopists).

**CVC-ClinicDB dataset** [43]: CVC-ClinicDB is an openly available collection of 612 images extracted from 31 colonoscopy sequences, with a resolution of  $384 \times 288$ . The dataset is commonly utilized in medical image analysis, specifically in detecting polyps in colonoscopy videos through segmentation techniques.

**CVC-ColonDB dataset** [44]: is provided by the Machine Vision Group (MVG). These images were extracted from 15 brief colonoscopy videos and consist of 380 images of  $574 \times 500$  pixels resolution.

**CVC-T dataset** [45]: CVC-T dataset is a subset of a larger dataset named Endoscene, and it is primarily a test set. It is composed of 60 images that were obtained from 44 video sequences captured from 36 patients.

**ETIS-Larib dataset** [46]: The dataset consists of 196 images with high resolution ( $1226 \times 996$ ).

#### 4.1.2 Upper GI tract dataset

There are three datasets we collected from endoscopy findings of patients at the Institute of Gastroenterology and Hepatology and Hanoi Medical University Hospital: the first for anatomical site classification, the second for lesion segmentation and classification, and the last for HP classification. They are combined into a huge dataset of the upper GI tract.

**Anatomical site dataset:** This dataset includes 5546 images of 10 anatomical sites, all of which are captured directly from the endoscopic machine, including four lighting modes: WLI (White Light Imaging), FICE (Flexible spectral Imaging Color Enhancement), BLI (Blue Light Imaging), and LCI (Linked Color Imaging). The images in this dataset do not contain any lesions and have labels specifying the anatomical site. Table 1 describes the details of this dataset.

Table 1: Number of images in each anatomical site and lighting mode

Anatomical site	WLI	FICE	BLI	LCI	TOTAL
Pharynx	177	134	120	119	550
Esophagus	169	141	116	127	553
Cardia	163	120	132	140	555
Gastric body	174	135	124	120	553
Gastric fundus	170	130	126	128	554
Gastric antrum	155	143	131	125	554
Greater curvature	171	131	126	125	553
Lesser curvature	155	140	134	126	555
Duodenum bulb	156	141	135	128	560
Duodenum	163	138	127	131	559

**Lesion dataset:** in this dataset, we have 4104 images of 5 types of lesions: reflux esophagitis, esophageal cancer, gastritis, stomach cancer, and duodenal ulcer. The images in this dataset have the annotations for both the classification and segmentation tasks. The numbers of images for reflux esophagitis, esophageal cancer, stomach cancer, and duodenal ulcer classes are 1335, 538, 1443, 538, and 250, respectively.

Figure 7 shows some samples in the lesion dataset.

**HP dataset:** we have 1819 images in this dataset, including HP-positive and HP-negative images. Figure 8 are some samples in the HP dataset.



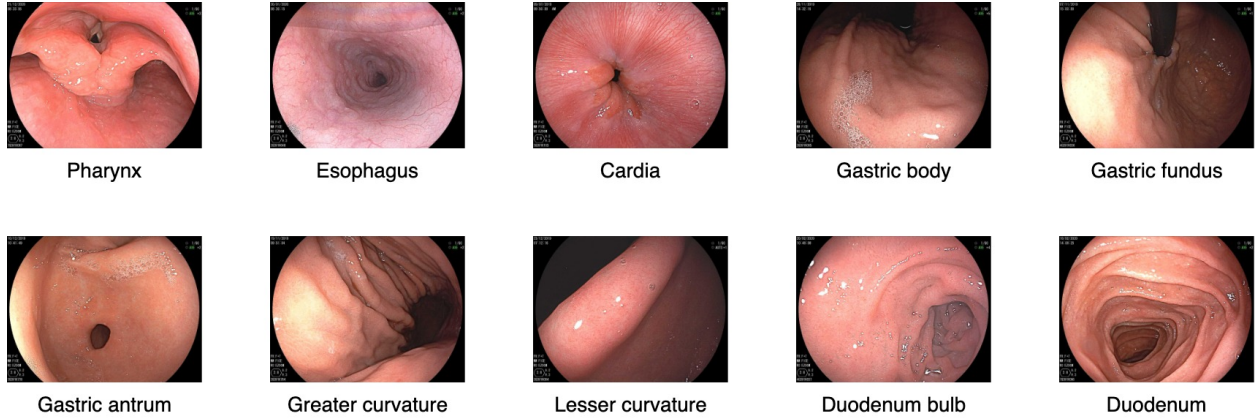


Figure 6: Some samples in anatomical dataset

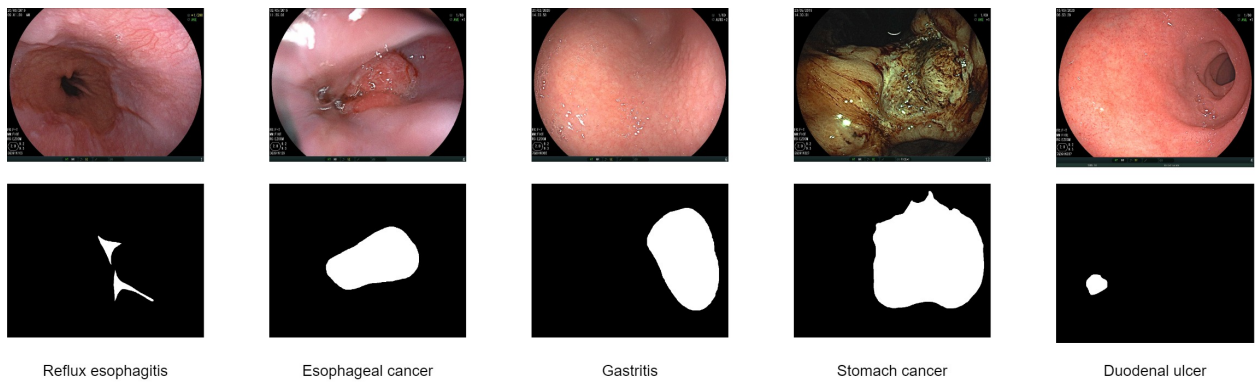


Figure 7: Some samples in lesion dataset

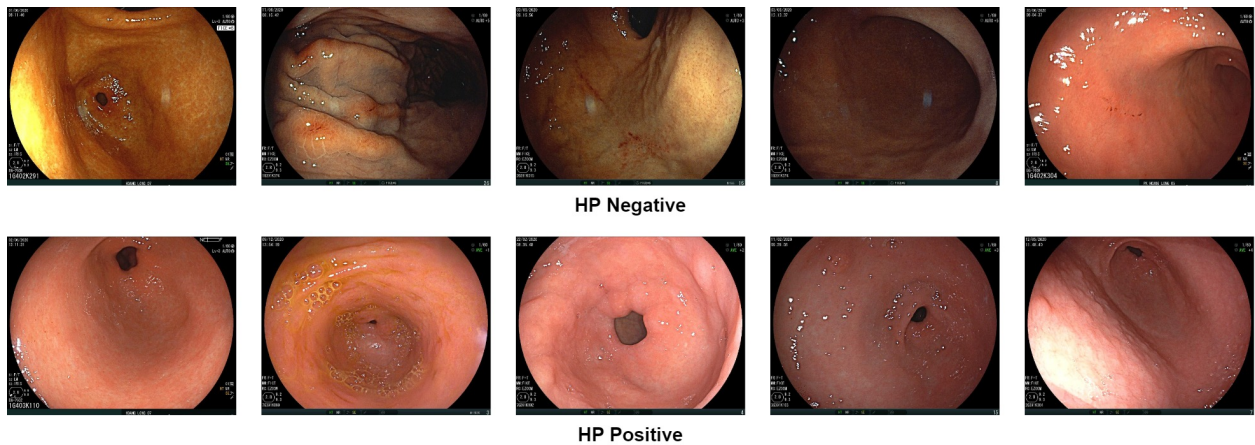


Figure 8: Some samples in HP dataset

## 4.2 Implementation Details

We performed two separate experiments on the upper GI and polyp datasets to validate our proposed UGCANet.

- **For polyp dataset:** For the polyp dataset, our approach utilizes an image size of 384x384 and employs multi-scale training with size ratios of 0.75, 1, 1.25, respectively. Regarding the optimization algorithm, we adopt Adam with an initial learning rate of 1e-4. Our data augmentation strategy comprises Flip, HueSaturation,

and RandomBrightnessContrast, each with a probability of 0.5. We perform three experiments with different dataset setups to compare with SoTA models.

**Experiment 1** : The splitting method recommended in [29] is applied, where 90% of the Kvasir and ClinicDB datasets are allocated for training. The remaining images in Kvasir and CVC-ClinicDB datasets, along with all images from CVC-ColonDB, CVC-T, and ETIS-Larib, are used for testing.

**Experiment 2**: 5-fold cross-validation on the CVC-ClinicDB and Kvasir datasets.

**Experiment 3**: Cross-dataset evaluation with three training-testing configurations:

1. CVC-ColonDB and ETIS-Larib for training, CVC-ClinicDB for testing;
2. CVC-ColonDB for training, CVC-ClinicDB for testing;
3. CVC-ClinicDB for training, ETIS-Larib for testing.

- **For upper GI dataset:**

5-fold cross-validation schema. The datasets are first divided into five subfolds, which are then merged to create larger folds. In the anatomical site dataset, each subfold consists of an equal number of images per anatomical site and lighting mode. Similarly, the lesion dataset’s subfolds contain an equal number of images per lesion type, and the HP dataset’s folds contain the same number of HP positive and HP negative samples. Additionally, a marker vector  $\mu$  is generated to denote the sample type.

We use two variants of the MiT backbone, namely MiT-B2 and MiT-B3, to conduct training on images of size 480x480 without utilizing multi-scale techniques. The Adam optimizer is utilized with a learning rate linear warmup and cosine strategy annealing.

The following experiments are performed to evaluate the model’s performance:

**Experiment 4**: we evaluate the impact of two MiT configurations on UGCANet, including MiT-B2 and MiT-B3, and compare their performance with backbones of EndoUNet [27], including VGG19, ResNet50, and DenseNet121.

**Experiment 5**: in the classification tasks, we train the single-tasking instances of models, including VGG19, ResNet50, DenseNet121, and MiT-B3, each of them trained on separate data. We compare the performance of multi-tasking models and the single-tasking models.

**Experiment 6**: in the lesion segmentation task, we train five single-tasking instances of EndoUNet and five single-tasking instances of UGCANet, each of which trained on separate lesion data. Then, we compare the performance of multi-tasking models versus the single-tasking instances.

All training is done on a machine with a 3.7GHz AMD Ryzen 3970X CPU, 128GB RAM, and an NVIDIA GeForce GTX 3090 GPU.

## 4.3 Results and Discussion

### 4.3.1 Comparison with SoTA methods

- **For polyp dataset:**

Table 2: Performance comparison of different methods on the Kvasir, ClinicDB, ColonDB, CVC-T and ETIS-Larib test sets. All results of UGCANet are averaged over five runs.

Method	Kvasir		CVC-ClinicDB		CVC-ColonDB		CVC-T		ETIS-Larib	
	mDice	mIOU	mDice	mIOU	mDice	mIOU	mDice	mIOU	mDice	mIOU
UNet [22]	0.818	0.746	0.823	0.750	0.512	0.444	0.710	0.627	0.398	0.335
UNet++ [23]	0.821	0.743	0.794	0.729	0.483	0.410	0.707	0.624	0.401	0.344
PraNet [29]	0.898	0.840	0.899	0.849	0.709	0.640	0.871	0.797	0.628	0.567
HarDNet-MSEG [47]	0.912	0.857	0.932	0.882	0.731	0.660	0.887	0.821	0.677	0.613
CaraNet [48]	0.918	0.865	0.936	0.887	0.773	0.689	0.903	0.838	0.747	0.672
TransUNet [25]	0.913	0.857	0.935	0.887	0.781	0.699	0.893	0.824	0.731	0.660
TransFuse-L* [26]	0.920	0.870	0.942	<b>0.897</b>	0.781	0.706	0.894	0.826	0.737	0.663
ColonFormer-S [49]	0.927	0.877	0.932	0.833	0.811	0.730	0.894	0.826	0.789	0.711
ColonFormer-L [49]	0.924	0.876	0.932	0.884	0.811	0.733	0.906	0.842	0.801	0.722
<b>UGCANet (Ours)</b>	<b>0.928</b>	<b>0.881</b>	<b>0.943</b>	<u>0.896</u>	<b>0.827</b>	<b>0.749</b>	<b>0.910</b>	<b>0.847</b>	<b>0.822</b>	<b>0.744</b>

Table 2 shows the comparison result for Experiment 1. Our model UGCANet outperforms previous SoTA models in mDice and mIoU metrics. Despite the impressive performance of ColonFormer-S on the Kvasir dataset, our model UGCANet outperforms ColonFormer-S and ColonFormer-L on the ETIS-Larib dataset by 2.1% in mDice and 2.2% on mIoU. On CVC-ColonDB, UGCANet surpasses TransFuse-L\* and TransUnet with 4.6% mDice and also mIoU of 5% and 4.3%, respectively. However, on our CVC-ClinicDB dataset, our model only approximates mDice and mIoU compared to TransFuse-L\*.

Table 3 shows us that UGCANet outperforms all state-of-the-art models in mDice, mIoU, precision, and even recall in the 5-fold cross-validation experiment on the ClinicDB dataset. With the Kvasir dataset, we continue to outperform other models on mDice and precision metrics. However, our model is 0.8% worse in recall and 0.1% in mIoU. It is worth mentioning that our UGCANet model has displayed remarkable stability on both datasets, with a relatively low standard deviation.

Table 3: Performance comparison of different methods on 5-fold cross-validation of the CVC-ClinicDB and Kvasir datasets. All results are averaged over 5 folds.

Dataset	Method	mDice	mIOU	Recall	Precision
ClinicDB	ResUNet++ [50]	0.815 ± 0.018	0.736 ± 0.017	0.832 ± 0.018	0.830 ± 0.020
	DoubleUNet [24]	0.920 ± 0.018	0.866 ± 0.025	0.922 ± 0.027	0.928 ± 0.017
	DDANet [51]	0.860 ± 0.014	0.786 ± 0.017	0.858 ± 0.023	0.892 ± 0.014
	ColonSegNet [52]	0.817 ± 0.020	0.873 ± 0.024	0.926 ± 0.025	0.933 ± 0.014
	HarDNet-MSEG [47]	0.923 ± 0.020	0.873 ± 0.024	0.926 ± 0.025	0.933 ± 0.014
	PraNet [29]	0.933 ± 0.012	0.884 ± 0.015	0.940 ± 0.005	0.937 ± 0.016
	ColonFormer-S [49]	0.948 ± 0.002	0.904 ± 0.004	0.958 ± 0.003	0.941 ± 0.004
	ColonFormer-L [49]	0.947 ± 0.002	0.903 ± 0.003	0.956 ± 0.002	0.942 ± 0.005
	<b>UGCANet (Ours)</b>	<b>0.950 ± 0.001</b>	<b>0.907 ± 0.003</b>	<b>0.959 ± 0.007</b>	<b>0.947 ± 0.012</b>
Kvasir	ResUNet++ [50]	0.780 ± 0.010	0.681 ± 0.008	0.834 ± 0.010	0.799 ± 0.010
	DoubleUNet [24]	0.879 ± 0.018	0.816 ± 0.026	0.902 ± 0.027	0.894 ± 0.039
	DDANet [51]	0.860 ± 0.005	0.791 ± 0.004	0.876 ± 0.015	0.892 ± 0.018
	ColonSegNet [52]	0.676 ± 0.037	0.557 ± 0.040	0.731 ± 0.088	0.730 ± 0.080
	HarDNet-MSEG [47]	0.889 ± 0.011	0.831 ± 0.011	0.892 ± 0.015	0.926 ± 0.014
	PraNet [29]	0.883 ± 0.020	0.822 ± 0.020	0.897 ± 0.020	0.906 ± 0.010
	ColonFormer-S [49]	0.924 ± 0.008	<b>0.875 ± 0.010</b>	<b>0.941 ± 0.010</b>	0.927 ± 0.008
	ColonFormer-L [49]	0.917 ± 0.006	0.865 ± 0.007	0.932 ± 0.007	0.926 ± 0.008
	<b>UGCANet (Ours)</b>	<b>0.926 ± 0.002</b>	<b>0.874 ± 0.003</b>	<b>0.933 ± 0.004</b>	<b>0.934 ± 0.003</b>

Table 5 compares UGCANet and other benchmark models regarding their size and computational complexity. Our model exhibits greater parameters than CNN-based models like CaraNet [48], or HarDNet-MSEG [47]. However, compared to the corresponding transformer architectures, our model proves advantageous in terms of parameter optimization. Despite having only a slightly higher computational complexity of 2.93 GFLOPs than ColonFormer-S [49], our model still outperforms it in terms of overall model performance.

- **For upper GI dataset:**

Our study investigated the effectiveness of various backbones in classifying lesions. According to Table 6, we found that model performance across datasets exhibits minimal variability. Notably, two datasets, anatomical site and lesion, demonstrated high accuracy rates. Even the lowest accuracies achieved by the single-tasking VGG19 model for anatomical site classification, lesion classification, and HP classification tasks were impressive at 97.07%, 98.51%, and 91.21%, respectively. However, our results indicate that multi-tasking models outperform single-tasking models. Particularly, SFMNet with MiT-B3 as the backbone and EndoUNet with Resnet50 as the backbone proved to be the top-performing models across all three tasks, achieving impressive accuracy rates of 98.46%, 99.63%, and 93.46%, respectively.

Table 7 exhibits the segmentation task results for the upper digest dataset. The multi-tasking model demonstrated superior performance to its single-tasking counterpart in most tests. Our investigation indicated that multi-tasking learning was notably more effective, particularly when utilizing the UGCANet model.

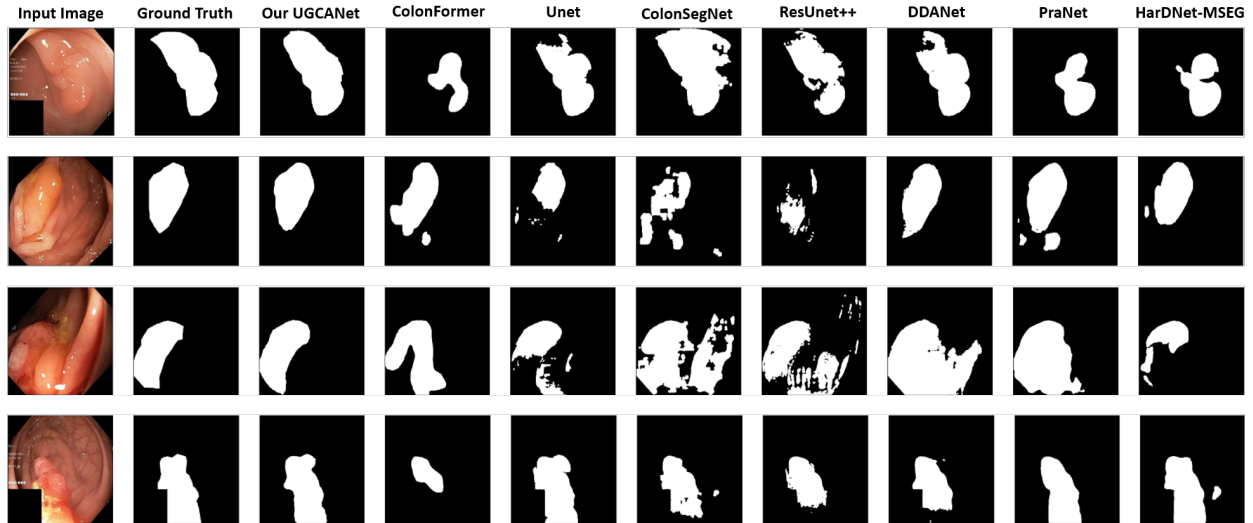


Figure 9: Qualitative result comparison of different models trained on the first fold of the 5-fold cross-validation on the Kvasir dataset.

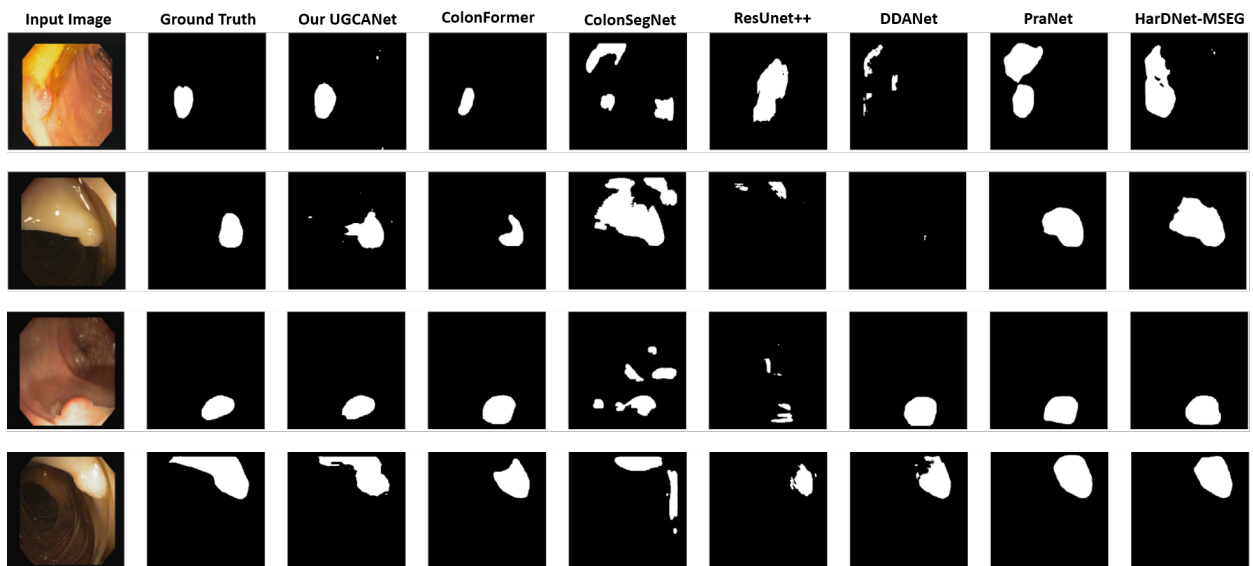


Figure 10: Qualitative result comparison using CVC-Colon for training and CVC-Clinic for testing.

#### 4.3.2 Ablation study

**Effectiveness of the FaPN:** At first glance, it is apparent that both SegFormer-B3 and MiT-B3-FaPN utilize the same backbone, MiT-B3, differing only in their respective decoders. Notably, the average mDice score of MiT-B3-FaPN is higher than that of SegFormer-B3, and the parameters and GFLOPs values displayed in Table 5 are significantly lower than those of MiT-B3-FaPN. The comparison results show that the computational cost with FaPN is much lower than that of SegFormer-B3 and the results are also slightly improved, so we choose FaPN as the decoder.

**Effectiveness of the CGNL:** By utilizing the CGNL module in addition, the ability to connect features by channels in groups of [38] is enhanced. Furthermore, the incorporation of channel attention, as opposed to MiT, yields a slight improvement in Table 8, particularly in the ClinicDB dataset, with an increase of approximately 1%.

**Effectiveness of the SE:** When replacing CGNL with SE, the results changed but not significantly. It seems that both modules add a channel attention mechanism to the MiT backbone to increase the representation of features.

Table 4: Performance comparison of different methods on cross-dataset configurations. All results are averaged over five runs.

Train	Test	Method	mDice	mIOU	Recall	Precision
CVC-ColonDB + ETIS-Larib	CVC-ClinicDB	ResUNet++ [50]	0.406	0.302	0.481	0.496
		ColonSegNet [52]	0.427	0.321	0.529	0.552
		DDANet [51]	0.624	0.515	0.697	0.692
		DoubleUNet [24]	0.738	0.651	0.758	0.824
		HarDNet-MSEG [47]	0.765	0.681	0.774	0.863
		PraNet [29]	0.779	0.689	0.832	0.812
		ColonFormer-S [49]	<b>0.851</b>	0.771	0.853	0.896
		ColonFormer-L [49]	0.847	0.770	0.844	<b>0.902</b>
		<b>UGCANet (Ours)</b>	<u>0.849</u>	<b>0.773</b>	<b>0.855</b>	<u>0.893</u>
CVC-ColonDB	CVC-ClinicDB	ResUNet++ [50]	0.339	0.247	0.380	0.484
		DoubleUNet [24]	0.441	0.375	0.423	0.639
		DDANet [51]	0.476	0.370	0.501	0.644
		ColonSegNet [52]	0.582	0.268	0.511	0.460
		HarDNet-MSEG [47]	0.721	0.633	0.744	0.818
		PraNet [29]	0.738	0.647	0.751	0.832
		ColonFormer-S [49]	<b>0.816</b>	<b>0.731</b>	0.809	<b>0.881</b>
		ColonFormer-L [49]	0.804	0.723	0.794	0.877
		<b>UGCANet (Ours)</b>	<u>0.809</u>	<u>0.724</u>	<b>0.822</b>	<u>0.870</u>
CVC-ClinicDB	ETIS-Larib	ResUNet++ [50]	0.211	0.155	0.309	0.203
		ColonSegNet [52]	0.217	0.110	0.654	0.144
		DDANet [51]	0.400	0.313	0.507	0.464
		DoubleUNet [24]	0.588	0.500	0.689	0.599
		PraNet [29]	0.631	0.555	0.762	0.597
		HarDNet-MSEG [47]	0.659	0.583	0.676	0.705
		ColonFormer-S [49]	0.723	0.635	0.797	0.731
		ColonFormer-L [49]	0.760	0.673	0.859	0.734
		<b>UGCANet (Ours)</b>	<b>0.803</b>	<b>0.722</b>	<b>0.905</b>	<b>0.766</b>

Table 5: Number of parameters and GFLOPs of different methods

Method	Parameters (M)	GFLOPs
PraNet [29]	32.55	13.11
HarDNet-MSEG [47]	33.34	11.38
CaraNet [48]	46.64	21.69
TransUNet [25]	105.5	60.75
TransFuse-L* [26]	-	-
SegFormer-B3 [40]	47.22	33.68
MiT-B3-FaPN	46.54	16.85
ColonFormer-S [49]	33.04	16.03
ColonFormer-L [49]	52.94	22.94
<b>UGCANet-S (Ours)</b>	46.22	18.96

**Combination of CGNL and SE:** After each feature group has learned internal information, the SE module combines and enhances its channel information. Our SFMNet performs best when the feature group and SE modules are utilized. Generally, the results of either the upper gastrointestinal dataset or the polyp dataset show a 1-2% improvement.

Table 6: Accuracy comparison on the three classification tasks

Method	Backbone	Anatomical site classification	Lesion classification	HP classification
VGG19 (cls only)	VGG19	97.07 ± 0.29%	98.51 ± 0.69%	91.21 ± 1.27%
Resnet50 (cls only)	Resnet50	97.53 ± 0.29%	98.79 ± 1.09%	91.87 ± 1.08%
DenseNet121 (cls only)	DenseNet121	97.65 ± 0.29%	99.16 ± 0.76%	91.81 ± 1.23%
MiT-B3 (cls only)	MiT-B3	97.58 ± 0.86%	99.45 ± 0.36%	91.43 ± 1.15%
EndoUNet	VGG19	98.09 ± 0.30%	99.58 ± 0.44%	93.13 ± 1.02%
	ResNet50	98.00 ± 0.49%	<b>99.63 ± 0.26%</b>	<b>93.46 ± 0.83%</b>
	DenseNet121	98.28 ± 0.50%	99.44 ± 0.75%	93.19 ± 1.14%
UGCANet	MiT-B2	98.30 ± 0.31%	99.11 ± 0.76%	93.35 ± 0.79%
	MiT-B3	<b>98.46 ± 0.41%</b>	99.54 ± 0.65%	93.29 ± 0.82%

Table 7: Dice Score comparison on the segmentation task

Method	Backbone	Reflux esophagitis	Esophageal cancer	Duodenal ulcer	Gastritis	Stomach cancer
UNet (seg only)	ResNet50	0.457 ± 0.011	0.807 ± 0.005	0.709 ± 0.021	0.444 ± 0.057	0.854 ± 0.021
SFM-based (seg only)	MiT-B3	0.515 ± 0.002	0.839 ± 0.012	<b>0.737 ± 0.008</b>	0.477 ± 0.051	<b>0.896 ± 0.009</b>
EndoUNet	VGG19	0.462 ± 0.014	0.807 ± 0.006	0.648 ± 0.024	0.419 ± 0.048	0.851 ± 0.009
	ResNet50	0.464 ± 0.006	0.819 ± 0.009	0.676 ± 0.024	0.443 ± 0.065	0.860 ± 0.009
	DenseNet121	0.474 ± 0.008	0.824 ± 0.007	0.670 ± 0.014	0.457 ± 0.066	0.866 ± 0.014
UGCANet	MiT-B2	0.493 ± 0.021	0.837 ± 0.012	0.704 ± 0.025	0.476 ± 0.074	0.885 ± 0.007
	MiT-B3	<b>0.517 ± 0.007</b>	<b>0.847 ± 0.012</b>	0.723 ± 0.009	<b>0.502 ± 0.072</b>	0.892 ± 0.008

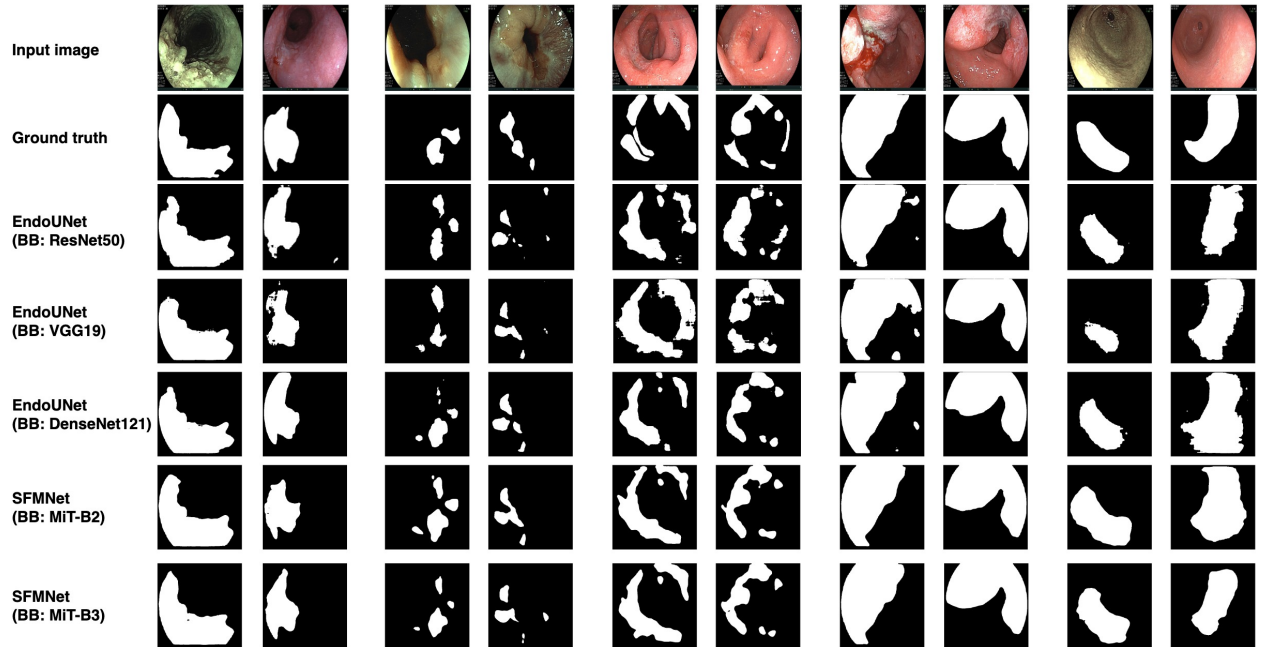


Figure 11: Some examples of the lesion segmentation task

Table 8: Ablation study on the effectiveness of the modules with **Experiment 1 of polyp dataset** setup. All results are averaged over five runs.

Method	Kvasir		CVC-ClinicDB		CVC-ColonDB		CVC-T		ETIS-Larib	
	mDice	mIOU	mDice	mIOU	mDice	mIOU	mDice	mIOU	mDice	mIOU
MiT-B3-FaPN	0.920	0.866	0.925	0.876	0.806	0.726	0.903	0.84	0.794	0.717
MiT-B3-CGNL-FaPN	0.923	0.875	0.934	0.888	0.811	0.733	0.906	0.842	0.817	0.738
MiT-B3-SE-FaPN	0.927	0.880	0.938	0.894	0.809	0.731	0.907	0.842	0.810	0.730
UGCANet	<b>0.928</b>	<b>0.881</b>	<b>0.943</b>	<b>0.896</b>	<b>0.827</b>	<b>0.749</b>	<b>0.910</b>	<b>0.847</b>	<b>0.822</b>	<b>0.744</b>

## 5 Conclusion

This study introduces a novel model called UGCANet that employs a Unified Global Context-Aware Transformer-based architecture. The proposed model demonstrates exceptional performance in addressing both multi-tasking and single-tasking problems. Our experimental findings indicate that UGCANet achieves state-of-the-art results in multi-tasking and exhibits competitive performance compared to prior segmentation approaches.

In future works, we plan to optimize the utilization of the FSM module to improve the performance of our method. The FSM and SE mechanisms differ only in their usage for the encoder and decoder. By potentially adjusting the FSM module or even the SE module, we can ensure that the model gains more comprehensive information before entering the decoder branch, resulting in enhanced outcomes.

## References

- [1] RL Siegel, KD Miller, and A Jemal. Cancer statistics, 2018. *CA: a cancer journal for clinicians*, 68(1):7–30, 2018.
- [2] L Liu, Y Liu, Q Wang, X Chen, and Q Wang. Automatic classification of colorectal polyps in ct colonography images. *Scientific reports*, 7(1):5556, 2017.
- [3] L Qin, J Li, L Zhang, and X Han. A computer-aided diagnosis system for colonic polyp classification based on deep learning. *Journal of medical systems*, 41(5):179–187, 2017.
- [4] H. Li, X. Li, J. Li, and Z. Li. Deep learning-based automatic polyp detection in colonoscopy videos. *Journal of Medical Systems*, 42(1):39–48, 2018.
- [5] K.W. Wong and S.K. Lo. A deep learning approach for polyp segmentation in colonoscopy images. In *International Conference on Medical Image Computing and Computer-Assisted Intervention*, pages 689–696. Springer, 2017.
- [6] R. Girshick, J. Donahue, T. Darrell, and J. Malik. Regional convolutional networks for accurate object detection and semantic segmentation. *arXiv preprint arXiv:1608.06993*, 2017.
- [7] T. Kooi, G. Litjens, B. E. Bejnordi, A. A. Setio, F. Ciompi, M. Ghafoorian, ..., and M. M. Wille. Large-scale annotated medical image databases for computer-assisted image analysis: a review. *IEEE Transactions on Medical Imaging*, 36(7):1515–1525, 2017.
- [8] K. He, G. Gkioxari, P. Dollár, and R. Girshick. Mask r-cnn. In *Proceedings of the IEEE International Conference on Computer Vision*, pages 2980–2988, 2017.
- [9] S. Huang, Z. Lu, R. Cheng, and C. He. Fapn: Feature-aligned pyramid network for dense image prediction. In *Proceedings of the IEEE/CVF International Conference on Computer Vision*, pages 864–873, 2021.
- [10] Jia Deng, Wei Dong, Richard Socher, Li-Jia Li, Fei-Fei Li, and Fei Fei-Fei. Imagenet: A large-scale hierarchical image database. *Computer Vision and Pattern Recognition, 2009. CVPR 2009. IEEE Conference on*, 2009.
- [11] Alex Krizhevsky and Geoffrey Hinton. Learning multiple layers of features from tiny images. *Computer Science*, 2009.
- [12] G. Huang, Z. Liu, L. van der Maaten, and K.Q. Weinberger. Densenet: Densely connected convolutional networks. *Proceedings of the IEEE Conference on Computer Vision and Pattern Recognition*, 1:4700–4708, 2017.
- [13] K. He, X. Zhang, S. Ren, and J. Sun. Resnet: Deep residual learning for image recognition. *Proceedings of the IEEE Conference on Computer Vision and Pattern Recognition*, 1:770–778, 2015.

- [14] Mingxing Tan and Quoc Le. Efficientnet: Rethinking model scaling for convolutional neural networks. In *International Conference on Machine Learning*, pages 6105–6114. PMLR, 2019.
- [15] Ashish Vaswani, Noam Shazeer, Niki Parmar, Jakob Uszkoreit, Llion Jones, Aidan N Gomez, Łukasz Kaiser, and Illia Polosukhin. Attention is all you need. *Advances in Neural Information Processing Systems*, 2017.
- [16] Alexey Dosovitskiy, Lucas Kolesnikov, Thomas Moeys, Matthias Backes, Jonas Beyer, and Jan Kautz. An image is worth 16x16 words: Transformers for image recognition at scale. *arXiv preprint arXiv:2010.11929*, 2020.
- [17] Wenhai Wang, Enze Xie, Xiang Li, Deng-Ping Fan, Kaitao Song, Ding Liang, Tong Lu, Ping Luo, and Ling Shao. Pyramid vision transformer: A versatile backbone for dense prediction without convolutions. In *Proceedings of the IEEE/CVF International Conference on Computer Vision*, pages 568–578, 2021.
- [18] Jianwei Yang, Chunyuan Li, Pengchuan Zhang, Xiyang Dai, Bin Xiao, Lu Yuan, and Jianfeng Gao. Focal attention for long-range interactions in vision transformers. In M. Ranzato, A. Beygelzimer, Y. Dauphin, P.S. Liang, and J. Wortman Vaughan, editors, *Advances in Neural Information Processing Systems*, volume 34, pages 30008–30022. Curran Associates, Inc., 2021.
- [19] Hugo Touvron, Matthieu Cord, Alexandre Sablayrolles, Gabriel Synnaeve, and Hervé Jégou. Going deeper with image transformers. In *2021 IEEE/CVF International Conference on Computer Vision, ICCV 2021, Montreal, QC, Canada, October 10-17, 2021*, pages 32–42. IEEE, 2021.
- [20] Ben Graham, Alaeldin El-Nouby, Hugo Touvron, Pierre Stock, Armand Joulin, Hervé Jégou, and Matthijs Douze. Levit: A Vision Transformer in ConvNet’s Clothing for Faster Inference. In *Proceedings of the IEEE International Conference on Computer Vision*, 2021.
- [21] Zhuofan Xia, Xuran Pan, Shiji Song, Li Erran Li, and Gao Huang. Vision transformer with deformable attention. In *Proceedings of the IEEE/CVF Conference on Computer Vision and Pattern Recognition (CVPR)*, pages 4794–4803, June 2022.
- [22] Olaf Ronneberger, Philipp Fischer, and Thomas Brox. U-net: Convolutional networks for biomedical image segmentation. In *International Conference on Medical Image Computing and Computer-Assisted Intervention*. Springer, 2015.
- [23] Zongwei Zhou, Jianlong Yao, Bihan Chen, Xiaojuan Xie, and Zongben Tu. Unet++: A nested u-net architecture for medical image segmentation. In *International Conference on Medical Image Computing and Computer-Assisted Intervention*. Springer, 2018.
- [24] Wei Li, Guotai Chen, Wei Wang, Shizhong Zhu, and Jie Tian. Doubleu-net: A multi-level u-net framework for medical image segmentation. In *International Joint Conference on Artificial Intelligence*. AAAI Press, 2019.
- [25] Jieneng Chen, Yongyi Lu, Qihang Yu, Xiangde Luo, Ehsan Adeli, Yan Wang, Le Lu, Alan L Yuille, and Yuyin Zhou. Transunet: Transformers make strong encoders for medical image segmentation. *arXiv preprint arXiv:2102.04306*, 2021.
- [26] Yundong Zhang, Huiye Liu, and Qiang Hu. Transfuse: Fusing transformers and cnns for medical image segmentation. In *International Conference on Medical Image Computing and Computer-Assisted Intervention*, pages 14–24. Springer, 2021.
- [27] Nguyen Duy Manh, Dao Viet Hang, Dao Van Long, Pham Cong Khanh, Nguyen Thi Oanh, Nguyen Thi Thuy, Dinh Viet Sang, et al. Endounet: A unified model for anatomical site classification, lesion categorization and segmentation for upper gastrointestinal endoscopy. In *2022 14th International Conference on Knowledge and Systems Engineering (KSE)*, pages 1–6. IEEE, 2022.
- [28] Liang-Chieh Chen, George Papandreou, Iasonas Kokkinos, Kevin Murphy, and Alan L Yuille. Deeplab: Semantic image segmentation with deep convolutional nets, atrous convolution, and fully connected crfs. *IEEE Transactions on Pattern Analysis and Machine Intelligence*, 40(4):834–848, 2017.
- [29] Deng-Ping Fan, Ge-Peng Ji, Tao Zhou, Geng Chen, Huazhu Fu, Jianbing Shen, and Ling Shao. Pranet: Parallel reverse attention network for polyp segmentation. In *International Conference on Medical Image Computing and Computer-Assisted Intervention*, pages 263–273. Springer, 2020.
- [30] Songtao Liu, Di Huang, et al. Receptive field block net for accurate and fast object detection. In *Proceedings of the European Conference on Computer Vision (ECCV)*, pages 385–400, 2018.
- [31] Hang Zhang, Kristin Dana, Jianping Shi, Zhongyue Zhang, Xiaoang Wang, Amrith Tyagi, and Amit Agrawal. Context encoding for semantic segmentation. In *Proceedings of the IEEE Conference on Computer Vision and Pattern Recognition*, pages 7151–7160, 2018.
- [32] Changqian Yu, Jingbo Wang, Chao Peng, Changxin Gao, Gang Yu, and Nong Sang. Learning a discriminative feature network for semantic segmentation. In *Proceedings of the IEEE Conference on Computer Vision and Pattern Recognition*, pages 1857–1866, 2018.



- [33] Tuan C. Nguyen, Thi Phuong Nguyen, Gia Huy Diep, Anh Hoang Tran-Dinh, Tran Viet Nguyen, and Minh Thang Tran. Ccbanet: Cascading context and balancing attention for polyp segmentation. In *Medical Image Computing and Computer Assisted Intervention - MICCAI 2021*, volume 12901 of *Lecture Notes in Computer Science*. Springer, Cham, 2021.
- [34] Hirotoishi Takiyama, Tsuyoshi Ozawa, Soichiro Ishihara, Mitsuhiro Fujishiro, Satoki Shichijo, Shuhei Nomura, Motoi Miura, and Tomohiro Tada. Automatic anatomical classification of esophagogastroduodenoscopy images using deep convolutional neural networks. *Scientific reports*, 8(1):1–8, 2018.
- [35] Yu-Wen Lin, Guo-Shiang Lin, and Sin-Kuo Daniel Chai. Helicobacter pylori classification based on deep neural network. In *2019 16th IEEE International Conference on Advanced Video and Signal Based Surveillance (AVSS)*, pages 1–5. IEEE, 2019.
- [36] Lianlian Wu, Jun Zhang, Wei Zhou, Ping An, Lei Shen, Jun Liu, Xiaoda Jiang, Xu Huang, Ganggang Mu, Xinyue Wan, et al. Randomised controlled trial of wisense, a real-time quality improving system for monitoring blind spots during esophagogastroduodenoscopy. *Gut*, 68(12):2161–2169, 2019.
- [37] Qi He, Sophia Bano, Omer F Ahmad, Bo Yang, Xin Chen, Pietro Valdastri, Laurence B Lovat, Danail Stoyanov, and Siyang Zuo. Deep learning-based anatomical site classification for upper gastrointestinal endoscopy. *International Journal of Computer Assisted Radiology and Surgery*, 15(7):1085–1094, 2020.
- [38] K. Yue, M. Sun, Y. Yuan, F. Zhou, E. Ding, and F. Xu. Compact generalized non-local network. In *Advances in Neural Information Processing Systems*, volume 31, 2018.
- [39] J. Hu, L. Shen, and G. Sun. Squeeze-and-excitation networks. In *Proceedings of the IEEE Conference on Computer Vision and Pattern Recognition*, pages 7132–7141, 2018.
- [40] E. Xie, W. Wang, Z. Yu, A. Anandkumar, J. M. Alvarez, and P. Luo. **Segformer**: Simple and efficient design for semantic segmentation with transformers. In *Advances in Neural Information Processing Systems*, volume 34, pages 12077–12090, 2021.
- [41] Xiaolong Wang, Ross Girshick, Abhinav Gupta, and Kaiming He. Non-local neural networks. In *Proceedings of the IEEE conference on computer vision and pattern recognition*, pages 7794–7803, 2018.
- [42] Ebesh Jha, Pia H Smedsrud, Michael A Riegler, Pål Halvorsen, Thomas de Lange, Dag Johansen, and Håvard D Johansen. Kvasir-seg: A segmented polyp dataset. In *International Conference on Multimedia Modeling*, pages 451–462. Springer, 2020.
- [43] Jorge Bernal, F Javier Sanchez, Gloria Fernandez-Esparrach, Debora Gil, Cristina Rodriguez, and Fernando Vilarino. Wm-dova maps for accurate polyp highlighting in colonoscopy: Validation vs. saliency maps from physicians. *Computerized Medical Imaging and Graphics*, 43:99–111, 2015.
- [44] Nima Tajbakhsh, Suryakanth R Gurudu, and Jianming Liang. Automated polyp detection in colonoscopy videos using shape and context information. *IEEE transactions on medical imaging*, 35(2):630–644, 2015.
- [45] David Vázquez, Jorge Bernal, F Javier Sanchez, Gloria Fernandez-Esparrach, Antonio M Lopez, Adriana Romero, Michal Drozdal, and Aaron Courville. A benchmark for endoluminal scene segmentation of colonoscopy images. *Journal of healthcare engineering*, 2017, 2017.
- [46] Juan Silva, Aymeric Histace, Olivier Romain, Xavier Dray, and Bertrand Granado. Toward embedded detection of polyps in wce images for early diagnosis of colorectal cancer. *International journal of computer assisted radiology and surgery*, 9(2):283–293, 2014.
- [47] Chien-Hsiang Huang, Hung-Yu Wu, and Youn-Long Lin. Hardnet-mseg: A simple encoder-decoder polyp segmentation neural network that achieves over 0.9 mean dice and 86 fps. *arXiv preprint arXiv:2101.07172*, 2021.
- [48] Ange Lou, Shuyue Guan, and Murray Loew. Caranet: Context axial reverse attention network for segmentation of small medical objects. *arXiv preprint arXiv:2108.07368*, 2021.
- [49] N. T. Duc, N. T. Oanh, N. T. Thuy, T. M. Triet, and V. S. Dinh. Colonformer: An efficient transformer based method for colon polyp segmentation. *IEEE Access*, 10:80575–80586, 2022.
- [50] Debesh Jha, Pia H Smedsrud, Michael A Riegler, Dag Johansen, Thomas De Lange, Pål Halvorsen, and Håvard D Johansen. Resunet++: An advanced architecture for medical image segmentation. In *2019 IEEE International Symposium on Multimedia (ISM)*, pages 225–2255. IEEE, 2019.
- [51] Nikhil Kumar Tomar, Debesh Jha, Sharib Ali, Håvard D Johansen, Dag Johansen, Michael A Riegler, and Pål Halvorsen. Ddanet: Dual decoder attention network for automatic polyp segmentation. In *ICPR International Workshop and Challenges*, 2021.
- [52] Debesh Jha, Sharib Ali, Nikhil Kumar Tomar, Håvard D Johansen, Dag Johansen, Jens Rittscher, Michael A Riegler, and Pål Halvorsen. Real-time polyp detection, localization and segmentation in colonoscopy using deep learning. *Ieee Access*, 9:40496–40510, 2021.